

Pathway to lowest-energy structures for the surface triple junction verified by machine learning

Authors: Yuan Fang,^{1,2,†} Ipen Demirel,^{3,†} Xiaopu Zhang,^{1,2,*} Yuchuan Shao,^{1,2} Jianda Shao,^{1,2} John J. Boland³

Affiliations:

¹Laboratory of Thin Film Optics, Shanghai Institute of Optics and Fine Mechanics, Shanghai 201800, China

²Key Laboratory of Materials for High Power Laser, Chinese Academy of Sciences, Shanghai 201800, China

³Centre for Research on Adaptive Nanostructures and Nanodevices (CRANN), AMBER SFI Research Centre and School of Chemistry, Trinity College Dublin, Dublin 2, Ireland

[†]These authors contributed equally

*Correspondence to: zhangxiaopu@siom.ac.cn

Abstract

The behavior of surface triple junctions (STJ) at emergent grain boundaries on free surfaces are critical contributors to material properties, particularly at the nanoscale. Interest has been stimulated by recent experimental observations of local grain rotation, the restructuring of emergent grain boundaries and the resultant levels of stress generation, and computationally by the introduction of the core-shift method for building wedge disclination structures at STJ and the establishment of relationships between atomic calculation and the continuum elastic theory. Despite this progress, the lowest-energy structure for the surface triple junction is still unknown. Here, we carried out the experimental observation of the local surface deformation at STJ, the local stress analysis and ergodic searches for metastable structures. We identified the zipped Y-shaped notch, rather than the zipped V-shaped notch or wedge disclination, as the most stable structures, which was subsequently verified with machine learning methods for a wide range of boundaries. Local stress analysis explains this energetic preference. Our findings provide fundamental insight into STJ energetics and offer a possible framework for understanding kinetically diffusive deformation and the pathway for engineering related material properties, in particular thin-film properties.

1. Introduction

Crystal defects such as grain boundaries (GB) and surfaces are critically important because they act as preferential sites for a wide range of processes that control the material properties, stability, and performance [1-3]. Surface triple junction (STJ) or emergent grain boundary (eGB) at the free surface is the intersection between GB and the surface, alternatively termination of GB at surface. Altogether, they provide short-circuit paths for rapid atomic transport and facilitate creep deformation; leading to void formation, cavities and intergranular fracture because of the local stress concentration, in addition to initiating preferential chemical reactions and intergranular corrosion. For example, in nanocrystalline interconnects in advanced integrated circuits, GB and its intersection with the hetero-interface play pivotal roles in determining electrical, thermal and mass transport properties and detrimental processes such as electromigration [4-7].

Research on low energy structures of GBs and eGBs at free surfaces, also called STJ [8, 9] and grain-boundary surface terminations [10], can provide a better understanding of GB related material properties especially for thin films of significantly technical importance [1, 11]. In recent years, great attention was paid to determine the stable and metastable structures of GBs, GB complexions and eGBs, through experimental, calculation and theoretical methods [12-20]. For example, the out-of-plane grain rotation in nanocrystalline copper films was observed and the GB energy driven core-shift

underlying this grain rotation was identified, which could play a significant role in the GB engineering and atomic scale manufacturing for the next generation integrated circuit [12, 13]. Grain-boundary phase transformation in elemental metal copper was also found, which suggests the possibility for material design [21-28]. The influence of metastable atomic structures on GB mechanical properties and diffusion clearly demonstrates the importance of the GB atomic structures [29, 30].

Zhang et al. recently observed the local out-of-plane grain rotation at certain eGBs with scanning probe microscope [14] and proposed a core-shift method to build and evaluate energetically restructured GBs at the free surface and the local stress generation [31, 32]. Boundaries with [112] rotation axes have the lowest boundary energy among boundaries obtained from the core-shift process in the $(1\bar{1}0)$ plane for (111) texture films [33]. Ignoring the transition region where the core changes direction, the core lies along the [112] direction in the close-packed plane close to the surface but lies along [111] direction in the bulk far below the surface. It can be viewed as a special kind of crack-like GB diffusion wedge in the absence of external stress [34-36] or an intrinsic crack-like GB diffusion wedge driven by the variation of the boundary structure and energy. The [112] eGB corresponds to a zipped chevron V-shaped notch or a wedge disclination in the continuum model and the quadratic relationship between the eGB energy and core shift (CS) depth has been established [31]. This very special relationship reconciled the atomic simulation results and the continuum elastic theory, and at the same time confirmed the mechanism of the energy balance between the boundary energy decrease and the elastic energy generation for [112] core-shifted boundaries [14].

The kinetics of this GB rotation with the rotation axes perpendicular to the tilt axes is probably achieved through atomic diffusion along the dislocation line and the consequent dislocation-line movement perpendicular to the Burgers vector or dislocation climb [13, 34, 35, 37-40]. In this process, the local rotation axis varies and the misorientation angle changes as well. In contrast, during grain rotation under an external stress field, as observed by Wang et al., the rotation axis remains the same while the misorientation angle varies [37, 41, 42]. The dislocation climb direction proposed by Gao et al. is along the film normal. Hence, it is perpendicular to that in the core-shift process and both are perpendicular to the Burgers vector [34-36].

Despite this progress, several problems have yet to be solved. First, the basic idea of the balance between the elastic energy and the interfacial energy, assumed in our previous paper [14], has not been demonstrated. Atomically, the boundary core of an eGBs can lie between [111] and [112]. It need not necessarily lie along the [112] direction in the close-packed plane, as reported previously [14, 31], and could even become curly. From the perspective of the continuum model, the eGB structure is not necessarily chevron V-shaped and thus it could have complex stress field. Secondly, there likely exists an unstable singular stress concentration at the tip of the chevron shaped wedge, as proposed by Gao et al. for unconstrained films under tensile stress [34-36]. Finally, the lowest energy eGB structures have yet to be identified.

In this paper, we first confirmed the local out-of-plane rotation for one small angle GB (13.17°) in a macroscopic copper bicrystal, where the global out-of-plane rotation is restricted. We analyzed the local virial stress at STJ, then revealed the singular stress localization at the wedge tips at an atomic level, and in the final step we lowered the eGB energy through blunting the wedge tip and delocalizing the stress field. We found that for a series of zipped Y-shaped notches emanating from the same chevron shaped notch, the eGB energy decays exponentially with the core-shifted depth.

At the same time, employing the core-shift method and instead of keeping the eGB axis along [112], we generated all possible metastable eGBs at a fixed core-shift depth to search for the lowest energy structures. For a given fixed core-shift depth we calculated, the eGB structure with the lowest energy is always coincident with the zipped Y-shaped notch. Since the number for all the possible core-shifted boundaries increases exponentially as a function of core-shift depth, in order to prove this hypothesis, we trained a machine-learning model with these eGB structures described by the core-shift sequence as inputs and their energies as outputs. The result demonstrated our hypothesis is valid with a high prediction accuracy.

This behavior indicates a fundamental tendency for a wide range of eGBs to restructure into zipped Y-shaped notches deep into the thickness of the film rather than speculated shallow zipped V-shaped notches or wedge disclinations. Given these enhanced defect penetration levels, we expect our observations are important to understand the plastic behaviour and atomic fracture mechanics of thin metal films and to predict the fracture behaviour at the atomic scale [34, 43].

2. Method

2.1 Grain boundary calculation

We focused on a symmetrical tilt GB with tilt axis $[111]$ and misorientation angle 13.17° or $2 \arctan(1/5\sqrt{3})$ in this paper, since there is only one dislocation core in each unit and hence the core-shift process is much simpler. The period vectors in the black and white crystals are $1/2 [\bar{3}\bar{2}5]$ and $1/2 [\bar{2}\bar{3}5]$, respectively. The boundary normal vectors in the black and white crystals are $1/2 [7\bar{8}1]$ and $1/2 [8\bar{7}\bar{1}]$, respectively, which implies the mean boundary plane is $(1\bar{1}0)$.

The molecular statics simulation were carried out with the LAMMPS software [44] and an embedded-atom-method potential for the copper developed by Mishin et al. and widely used for the defect properties of copper [45]. The atomic stress was calculated according to the virial theorem [46]. The calculated atomic structures are visualized with OVITO software [47].

GBs are calculated with periodic boundary conditions in three directions, the rotation axis, period vector and boundary normal, and each repeat cell contains a pair of parallel GBs of equal and opposite misorientation [48]. The relaxed configuration for the copper GBs is obtained by a conjugated-gradient energy minimization with respect to both the atomic coordinates and the simulation cell size along the boundary normal direction. The boundary structure searches were done with hundreds of different in-plane displacements as the initial configuration. Only the lowest-energy structures are considered to build further the suspended films for eGB research. After the relaxation of the boundary with three atomic layers along the tilt axis $[111]$, the bottom layer is labelled as A and the top one C. We built the suspended film through stacking the relaxed three-atomic-layers together and then adding the vacuum layer. More detailed information could be found in our previous work elsewhere [31].

2.2 Emergent grain boundaries and core-shift method

The core shift method was used in this paper, as shown in Fig. 1. Figure 1a shows the out-of-plane grain rotation from the black bicrystal to the red bicrystal and consequent GB core shift with an angle $\sim\psi$. The tilt axis for the black bicrystal is $[111]$ and the misorientation angle θ . The two black half-bicrystal were rotated along the x axis $\varphi/2$, clockwise and anti-clockwise, respectively. The tilt axis shifts an angle ψ from $[111]$ towards $[112]$ or even further in the $(1\bar{1}0)$ plane. The core shift process in a single atomic plane perpendicular to the tilt axis can be achieved by removing (see Fig. 1b) or adding atoms. Clearly the dislocation line movement direction is perpendicular to the Burgers vector and hence the core-shift process is a special kind of dislocation climb. The shifted GB core can be clearly seen in the GB plane, as shown in Fig. 1c. Figure 1d shows a perspective view of the core-shifted emergent boundary for GB $[111]$ 13.17° . The step-by-step process to build a $[112]$ CS boundary is shown in Fig. 1e. The top, middle and bottom panels are projected along the tilt axis, the boundary normal and the period vector, respectively. Below each three-view visualization the corresponding cross-sectional view is shown. The atoms to be deleted in each step were located between the two red arrows marked in the graph.

The labelling system details both the depth of the core shift and the number of deleted atoms. For example, the core shift depth (CSd) for the second structure in Fig. 1e is the top 3 layers, the number of the deleted atoms (DA) is 3, and the stacking fault depth is 6 atomic layers. We denote this structure as CSd3DA3. To build CSd6DA9 from CSd3DA3, 6 atoms between two red arrows in the middle panel of the cross-section view have to be deleted. The perspective view of the structure CSd9DA18 is shown in Fig. 1d. Atomically, the number of deleted atoms each layer in the first ABC stacking unit

of CSd3DA3 is 1, which also means the core in the first ABC stacking unit was shifted one time. The number of deleted atoms each layer in the first ABC stacking unit for CSd6DA9 is 2, and that in the second ABC stacking unit is 1. This means that the core in the first ABC stacking unit was shifted two times and that in the second ABC stacking unit was shifted one time. Similarly, the number of deleted atoms each layer in the first, second, third ABC stacking unit for CSd9DA18 is 3, 2, 1, respectively. The numbers of deleted atoms each layer in the first, second, third, fourth ABC stacking unit for CSd12DA30 are 4, 3, 2, 1, respectively.

2.3 Machine learning method

Machine learning techniques are widely used in research areas such as material design [49-51] and GBs [52-56]. Here, we used scikit-learn Python library to implement the machine learning algorithm [57]. The machine learning implementation flowchart is shown in Fig. 2. It contained six main steps, these are: data collection, feature selection and descriptor, algorithm, training and evaluation, machine learning model, and prediction. Our enumerated eGB structures and their energy form the dataset (see Tab. S1-2). We chose the core shift times or number of deleted atoms for each ABC stacking unit as the key features and the sequence of the core-shift times from top surface as the descriptor. Different algorithms were employed such as neural network of different layers, random forest and least square regressions of different orders, as shown in Fig. S1-2. For the machine learning algorithm of least square regression, the explicit expression for the model was also exploited. For model training, the whole data sets are divided into training sets and test sets by random sampling. The training data sets contained 80% of all the data and the rest belong to the test sets.

3. Results and discussion

3.1 Experiment

Considering an eGB structure at the fixed depth in the continuum theory, as shown in Fig. 1a, the out-of-plane rotation with a certain angle shifts the combined rotation axis from [111] toward [112] in the $(\bar{1}\bar{1}0)$ plane. The eGB defect energy is the balance of the GB energy and resulting elastic energy consequently generated. For the [112] core shifted eGBs, the GB energy reaches the lowest value [33]. However, in this case, the elastic energy $G/(4\pi(1-\nu)) \cdot \varphi^2 h^2$ for the wedge disclination corresponding to the zipped chevron V-shaped notch is generated, where G is the shear modulus, ν the Poisson ratio, φ the out-of-plane rotation angle of the core shifted eGB, and h the fixed depth [31]. Since the GB energy decreases monotonically as the out-of-plane rotation angle increases towards φ , there is a need to balance the boundary energy and the elastic energy with an out-of-plane rotation angle between 0 and φ .

Since there are four non-equivalent dislocation cores in each period for the emergent boundary with [111] tilt axis and the 26.01° misorientation angle previously reported [14], it is too complex to be taken as an example to show the energy balance scheme [14]. Hence, we designed a macroscopic bicrystal sample with [111] tilt axis, 13.17° misorientation, 8 mm diameter and 2 mm thick, as shown in Fig. 3a [31]. The experimental method employed for GB [111] 13.17° is the same as that for GB [111] 26.01° , as described before [14]. There is only one dislocation core in each period for this emergent boundary or five close-packed atomic lines, as analysed in our previous paper [31]. Experimentally, the eGB also exhibits local grain rotation from the perspective view and line profiles, as shown in Fig. 3b-c. While the local grain rotation is evident, the dissociation width is close to the local rotation width, which is a little different from that for the surface profile of GB [111] 26.01° . Hence, we take GB [111] 13.17° as an exemplar to search the lowest-energy structure.

3.2 Cell size effect

Before searching for the lowest energy structure, we first carried out simulations with the core-shift method and calculated the eGB energy with different cell sizes along the boundary normal direction, to remove any artificial effects due to the boundary interaction between two GBs in each simulation cell. The cell sizes along the boundary normal are 3, 5, 10, 15, and 20 times the magnitude of the

boundary normal. The quadratic term of the parabolic curves involves the elastic energy and it is influenced by the boundary interaction, as shown in Fig. 4a. Through parabolic fitting, we obtained the coefficient for the quadratic term. It is clear that there is boundary interaction when the cell size along the boundary normal is less than 10 times the boundary normal magnitude. Otherwise, the coefficient saturated to the value ~ 0.041 , consistent with our previous calculation, and hence the effect of boundary interaction can be neglected. The relationship between the core-shift depth CSd and the wedge depth h for the continuum disclination model $h = (CSd + 1.5) \cdot a/\sqrt{3}$ was established in the previous paper and are plotted in the upper and lower horizontal X-axes in Fig. 4 [31]. In the simulations below, we took the simulation cell size along the boundary normal to be 15 times the boundary normal magnitude.

The relaxation effect of the simulation cell along the boundary normal is also shown in Fig. 4b. The black curve and the red curve show the eGB energy without and with the simulation cell relaxation, respectively. The relaxation reduces each eGB energy slightly. The thickness effect was also examined, taking GB [111] 9.43° for example. We calculated core-shift depth dependent eGB energy at three different film thickness, that is 80, 120 and 160 ABC-stacking units, as shown in Fig. 4c. Clearly, another free surface helps the system to relax further. To avoid this effect, we used the film of a sufficient thickness with 160 ABC-stacking units. In summary, the size effects are removed by increasing the thickness of the suspended films and increasing the spacing between two equal and opposite boundaries in each simulation cell.

3.3 Local stress analysis

We firstly performed a local stress analysis in order to reduce the local elastic energy. A wedge disclination with tilt axis [112] near the surface and tilt axis [111] deep into the film was built previously and corresponds to a perfect chevron V-shaped notch in the continuum model. We immediately noticed the similarity to the crack-like GB diffusion wedges subjected to external stress for the eGB in metal films proposed almost three decades ago by Gao [34] and other related models [58, 59]. The analysis there shows a singular stress concentration near the wedge tip that is similar to the case in a crack, but shows a stress concentration at the wedge opening. In contrast, a real crack opening is nearly stress-free [36, 39, 60].

Considering the core-shift method, these low energy [112] core-shifted GBs, and their relationship with the continuum wedge disclination model, we analysed the hydrostatic stress field at different core shift depths, as shown in Fig. 5, during the low energy structure search. All images were colored with atomic hydrostatic stress from -0.5 GPa to 0.5 GPa. The blue atoms are under compressive stress and the red atoms are under tensile stress. The core shift depth is followed by the total number of deleted atoms. The atomic structures for CSd0DA0, CSd3DA3, CSd6DA9, CSd9DA18, CSd12DA30 were shown in Fig. 1e and the corresponding eGB energy was shown in Fig. 4b. The white arrows in Fig. 5 identified the deepest core-shifted layer. Clearly, the hydrostatic stress field transitioned from tension above the arrow to compression below the arrow. In the continuum wedge disclination model, the corresponding wedge depth and the chevron V-shaped notch depth is $h = (CSd + 1.5) \cdot a/\sqrt{3}$. It makes sense that the upper closed or zipped region is under tension and the tip of the chevron V-shaped notch is under compression in continuum mechanics due to the shear deformation involved during zipping up the chevron V-shaped notch [14, 61]. From these images, it is clear the compressive stress at the wedge tip is much more localized than the tensile stress at either side of the wedge opening.

We found similar singular stress concentrations at the wedge tips for all [112] core-shift eGBs. Since the elastic energy is quadratic in the stress, it is possible to lower the system energy by delocalizing the stress.

3.4 Zipped Y-shaped notches

To fulfill the above analysis, we delocalized the stress concentration by blunting the wedge tip by transforming it into a zipped Y-shaped notch. The blunting process for a [112] core-shifted eGB derived from GB [111] 13.17° is shown in Fig. 6a. We took as an example the structure CSd15DA30,

which is [112] core-shifted emergent boundary. The numbers of deleted atoms each layer in the first, second, third, fourth, and fifth ABC stacking unit for CSd15DA33 are 4, 3, 2, 1, and 1, respectively. The numbers of deleted atoms each layer in the first six ABC stacking units for CSd18DA36 are 4, 3, 2, 1, 1, and 1, respectively. The numbers of deleted atoms each layer in the first seven ABC-stacking units for CSd21DA39 are 4, 3, 2, 1, 1, 1, and 1, respectively. The remaining eGBs in the list can be analyzed similarly.

If we consider the wedge disclination for [112] core-shifted eGBs as the zipped chevron V-shaped notch CSd12DA30 shown in first panel in Fig 6(a), the remaining panels show the progressive formation of zipped Y-shaped notch structures. The core-shifted eGB energy as a function of the core-shift depth for the zipped Y-shaped notch emanating from CSd12DA30 was shown as the blue curve in Fig. 6b. It decreases monotonically. The longer the vertical stem of the Y-shaped notch, the lower the corresponding eGB energy, shown as successive blue points along the blue curve. Note that the [112] core-shifted eGB energy itself is shown as the red parabola-like curve in Fig. 6b. We also carried out computation on the eGB energy of the Y-shaped notch structures emanating from other [112] core-shifted eGBs, and similar behavior was found.

We always observed a monotonic change in energy while increasing the vertical stem length of the zipped Y-shaped notch regardless of whether or not we started with the lowest energy zipped V-shaped notch (CSd=12). In some cases, for example CSd=3 and 6 the black and yellow curves in Fig 6(b) the energy increased monotonically while for CSd =9, 12, 15 and 18 (orange, blue, purple and green in order), it decreased monotonically. The transition depth is between 6 layers and 9 layers. We found that all the curves can be well fitted to an exponential formula $\varepsilon = \varepsilon_{ex} + A \cdot \exp(-csd/\xi)$, where the ε_{ex} is the extrapolated value for the eGB energy, A the amplitude, and ξ the decay length in atomic layer unit. The amplitude A changes polarity at the transition depth. The lowest extrapolated value for the eGB energy is -0.235 nJ/m and the decay length is ~ 9 atomic layer. The corresponding [112] core-shift GB is CSd12DA30 and the corresponding curve in Fig. 6b is blue.

In addition to the emergent boundary eGB [111] 13.17° , we also carried out simulation on eGB [111] 9.43° and eGB [111] 3.89° . They exhibit the same behaviour for the [112] core-shift boundaries, as shown in Fig. 7(a-b). The group of zipped Y-shaped notches emanating from the same [112] core shifted boundary also show exponential relation between the eGB energy and core-shift depth. The transition depth highlighted by the arrows for eGB [111] 3.89° and eGB [111] 9.43° are a value between 9 and 12, and 9, respectively. Comparing the three emergent boundaries, the transition depth hardly depends on the misorientation. In addition, the transition depth is clearly different from the apex depth with lowest eGB energy on the parabolic curves. Both suggest the transition depth is a result of surface effects.

To find the principle underlying for the monotonic energy decrease of the eGB structure shown in the curves in Fig. 6b, the zipped Y-shaped notch with CSd=12 was scrutinized. We calculated the atomic scale stress for three structures, CSd12DA30, CSd18DA36, CSd24DA42, corresponding to different points along the blue curve in Fig. 6b. The results are shown in Fig. 6c. It is clear that when the stem of the Y-shaped notch becomes longer, both the stress intensity and the area are reduced significantly, in particular the compressive stress intensity and its corresponding area. For example, the numbers of deleted atoms each layer in the first few ABC stacking units from the top surface for CSd12DA30 are 4, 3, 2, and 1, respectively. The numbers of deleted atoms each layer in the corresponding ABC stacking unit from the top surface for CSd18DA36 are 4, 3, 2, 1, 1 and 1, respectively, and for CSd18DA42 they are 4, 3, 2, 1, 1, 1 and 1, respectively.

Our results above show clearly that in most cases the wedge disclination corresponding to the zipped chevron V-shaped notch with the depth greater than the transition depth is not the lowest energy structure. Instead, the eGB defect restructures into a zipped Y-shaped notch with an even lower defect energy. However, the lowest eGB structures for a certain core shift depth are still unknown, considering the large numbers of metastable structures.

3.5 Energy balance, enumeration and anticipation

Instead of searching for the lower energy eGB structures through delocalizing the stress field in the atomic calculation, an alternative approach involved fixing the core-shift depth and enumerating all the possible core-shift combinations to find the stable eGB structures. This method works well, in particular for shallow core shift depths. The results are shown in Fig. 8. Figure 8a shows all the possible eGB structure from the lowest energy toward the highest energy, obtained with the core-shift method at a fixed core shift depth $CSd = 12$, which means there are no atoms deleted from layers deeper than this. Note that two eGB structures, CSd12DA18 and CSd12DA27 (circled in red in Fig. 8b), share nearly the same eGB energy even with different numbers of jogs in the eGB stacking fault ribbon. The less point defects along the eGB stacking fault ribbon generally corresponds to the eGB close to [112] core shifted one and less elastic energy. Evenly distributed point defects rather than the agglomerated point defects along the eGB stacking fault ribbon generally lower the system elastic energy. Since the elastic energy is not only dependent on the number of jogs but also their relative position and the system energy includes both the GB energy and the elastic energy [62, 63], there is no simple way to estimate the total eGB energy from the structures in Fig. 8a.

The numbers of eGB structures in total for a fixed core shift depths of 3, 6, 9, 12, 15, 18, 21 layers are 1, 2, 4, 8, 16, 32, and 64, respectively. We did not carry out ergodic simulations for lowest energy eGB structures for a fixed core shift depth greater than 21 layers due to the exponentially increasing number of structures and consequently the huge amount of computation work required. To ensure that we have listed all the possible metastable core shift structures, we developed an enumeration rule. Our calculation shows that metastable core shift structures can be obtained only when the core-shift times for the ABC stacking unit above is the same as the that below or 1 more than that below. Accordingly, the total numbers of eGB structure at certain core shift depth is $2^{(csd/3)-1}$. For example, the number of eGB structures for a fixed core shift depth 21 is $2^{(21/3)-1} = 64$, which is the same as that in the enumeration method. It indicated that we indeed have listed all the possible core-shifted structures. Furthermore, we also tested eGB structures violating the enumeration rule and found eGB energies are always increased greatly.

The enumeration approach is validated by the coincidence of the lowest eGB energy at certain core-shift depth with the asymptote of the exponential curve describing the zipped Y-shaped notches emanating from each zipped V-shaped notch, such as that described in Fig 8(b). We further anticipated that the lowest energy structures, at depth greater than the vertex depth involving the bottom of the parabolic curves for the [112] CS boundary, correspond to the data point along the exponential line. Apart from the above analysis, we noticed that other clear patterns emerged in Fig. 8b. For example, the exponential relationship shown in Fig. S3 and by further examination we found this group of structures shared the same notch shape.

We summarized our research graphically for an eGB with the local tensile stress, as shown in Fig. 8c. There is a natural transition of the stable eGB structure from the zipped V-shaped notch to zipped Y-shaped notch. For either the V-shaped notch or the Y-shaped notch, the continuum model includes four steps: these are the initial structure, cut-out, zipping and final structure with local tensile stress. In one extreme case, the V-shaped notch dominates, as proposed by Gao, et al [34]. In other extreme case, the Y-shaped notch is deep down into the bottom of the films, which is the case proposed by Chason, et al [64-66].

3.6 Machine learning training, model and prediction

To predict the energy for different eGB structures at core shift depths beyond 18 layers, we built a machine learning model. It includes four main steps. The first step is data collection from LAMMPS calculation as we described and analysed above. The remaining three steps are detailed below.

The second step is to select the feature to represent our eGB structures. From the above analysis, it is clear that the core-shift times for each ABC stacking unit is one option. The descriptor for one eGB structure is then the sequence of its core-shift numbers, one number for each ABC stacking unit. The

dimension of the descriptor is the number of ABC stacking unit involved in the core-shift process. The eGB energy is the corresponding label value for this eGB structure. For example, the descriptor or the feature vector for the second structure in Fig. 8a is a vector [4, 3, 2, 1], corresponding to a number 4321, for the training of a 4-dimensional model. The corresponding descriptor was transformed into [4, 3, 2, 1, 0, 0] for the training of a 6-dimensional model through dimensionality increment, corresponding to a number 432100.

The third step was to select the machine learning algorithm. We tried single layer neural network, random forest and different kinds of least square regression such as linear, polynomial, logarithmic and exponential prototypical function. For the neural network model, we adopt one hidden layer with 70 thousand neurons after trialing with several different parameters. For random forest model, the number of trees in the forest is 50. For the regression algorithm, the best result is obtained with the polynomial function of the descriptors and the degree 2, or second order polynomial. Hence, only the results from least square regression with degree 2 were shown below.

The fourth step was to train a model and evaluate the model. The performance of the model is evaluated by the root mean square error (RMSE), the determination coefficient R^2 and comparison with calculated values with LAMMPS.

Figure 9a shows the comparison between the calculated values and the predicted values from machine learning models with three different algorithms, as a function of the numerical order. The eGB structures were ordered according to the corresponding numbers of the descriptor vectors. There are $2^6 = 64$ predicted data points in total for core-shift depth 21 (see Tab. S3). The machine learning model is obtained from the training dataset for core shift depth 3, 6, 9, 12, 15, and 18. It includes all the data with CSd less than 21 and the additional 6 data points on the exponential lines with CSd=21 in Fig. 8b. The total number of data is $\sum_{i=0}^5 2^i + 6 = 69$. The green data shows the calculated data with molecular statics method. It is clear that predicted data from least square regression algorithm and random forest algorithm looks much better than that from the neural network.

To qualitatively address the prediction accuracy and performance of different algorithms, we plotted out the predicted eGB energy as a function of the calculated eGB energy and calculated the determination coefficient for different algorithms, as shown in Fig. 9b. The determination coefficient R^2 is calculated with the testing data only. The solid line is the perfect fitting and dashed lines show $\pm 0.02 \text{ nJ} / m$ away from the perfect fitting. From the plot, obviously the least square regression algorithm underestimates the eGB energy and works quite well in all range of the eGB energy, while the random forest overestimates the eGB energy the low energy eGB energy and severely underestimates the eGB energy for high energy eGB energy. The data points from the neural network prediction scatters around both sides of the perfect fitting line. The RMSE for least square regression, random forest, and neural network are $0.0028 \text{ nJ} / m$, $0.0134 \text{ nJ} / m$ and $0.0173 \text{ nJ} / m$, respectively. The determination coefficient for least square regression, random forest, and neural network are 0.996, 0.917, and 0.860, respectively, which indicates that the least square regression is the best choice.

3.7 Verification

To predict the eGB energy and verify our anticipation, we trained other models with all the data with core-shift depth no more than 21 with a descriptor vector dimension no more than 7. Since the high determination coefficient of the least square regression of degree 2, we trained new model with this algorithm only. For example, to predict the eGB energy with dimension 8 with CSd 24, we transformed the descriptors by increasing the dimension of all the data with CSd less than 24 into 8 by add zero at the end of the descriptor vectors and add the 6 points with dimension 8 on the exponential lines. The predicted results were shown in Fig. 10a. The global minimum energies are indicated by arrows, which is one of the circled data points on the exponential lines in Fig. 8b.

Similarly, we increased the descriptor vector dimension again, add 6 more available data points with CSd=27 on the exponential lines, and then trained a new model for CSd no more than 27 and dimension 9. The predicted energy for all the structures with CSd=27 is shown in Fig. 10b and the minimum

energy is highlighted with arrow. This energy is also located on the exponential line in Fig. 8b and the structure corresponds to the zipped Y-shaped notch.

To obtain a new model for CSd no more than 30 and descriptor vector dimension 10, we add 18 data points on the exponential lines with CSd=24, CSd=27 and CSd=30 to the previous training dataset with CSd no more than 21. The predicted energy for all the structures with CSd=30 is shown in Fig. 10c and the minimum energy is highlighted with arrow. This energy is also located on the exponential line in Fig. 8b and the structure corresponds to the zipped Y-shaped notch as well. At last, we added all the predicted data with CSd=24, 27, 30 into the plot shown in Fig. 10d. Clearly that the lowest-energy structures for STJs are all located on the blue exponential curve.

The explicit expressions with the algorithm of least square regression were analysed. The coefficient for the four models obtained above are very similar, which is detailed in Tab. S4-7 in Supplementary Materials.

3.8 Discussion

Diffusive processes associated with atoms entering and exiting the GBs and the transformation from zipped V-shaped notches into zipped Y-shaped notches are intrinsically linked to the GB transformation [16, 21, 23, 30, 67, 68]. Under different constraints such as thermal treatment, external force field and atom flux, the free energy of eGB structure vary and hence eGB keep restructuring themselves through eGB transformation and boundary transformation.

It is reported that when diffusional deformation processes such as GB diffusion or surface diffusion dominates over dislocation plasticity, a crack-like GB diffusion wedge forms under the tensile force along the boundary normal [34]. The wedge generates a stress field with crack-like singular stress concentration at its tip. This singular stress field promotes the dislocation nucleation at the root of the grain boundary. In contrast, our finding shows that when the stem of a zipped Y-shaped notch rather than the tip of the zipped V-shaped notch reaches the interface between the film and the supporting substrate, the structure decomposed into a single parallel-glide dislocation and a new zipped Y-shaped notch [34]. Then the parallel gliding of the parallel-glide dislocation takes place [34, 43]. The necessary stress for the parallel-glide dislocation nucleation is expected to decrease greatly.

Finally, the discovery of the intrinsic crack-like GB diffusion wedge in the absence of external stress field highlights the energy transformation between defect structures and local stress distribution and may prompt a re-evaluation of the tensile or compressive stress generation [58, 64, 65, 69, 70] and even the Griffith fracture theory at the atomic scale. This is particularly relevant for the scenarios where the eGBs can survive, such as in nanoscale devices and the additive manufacturing in the outer space [71].

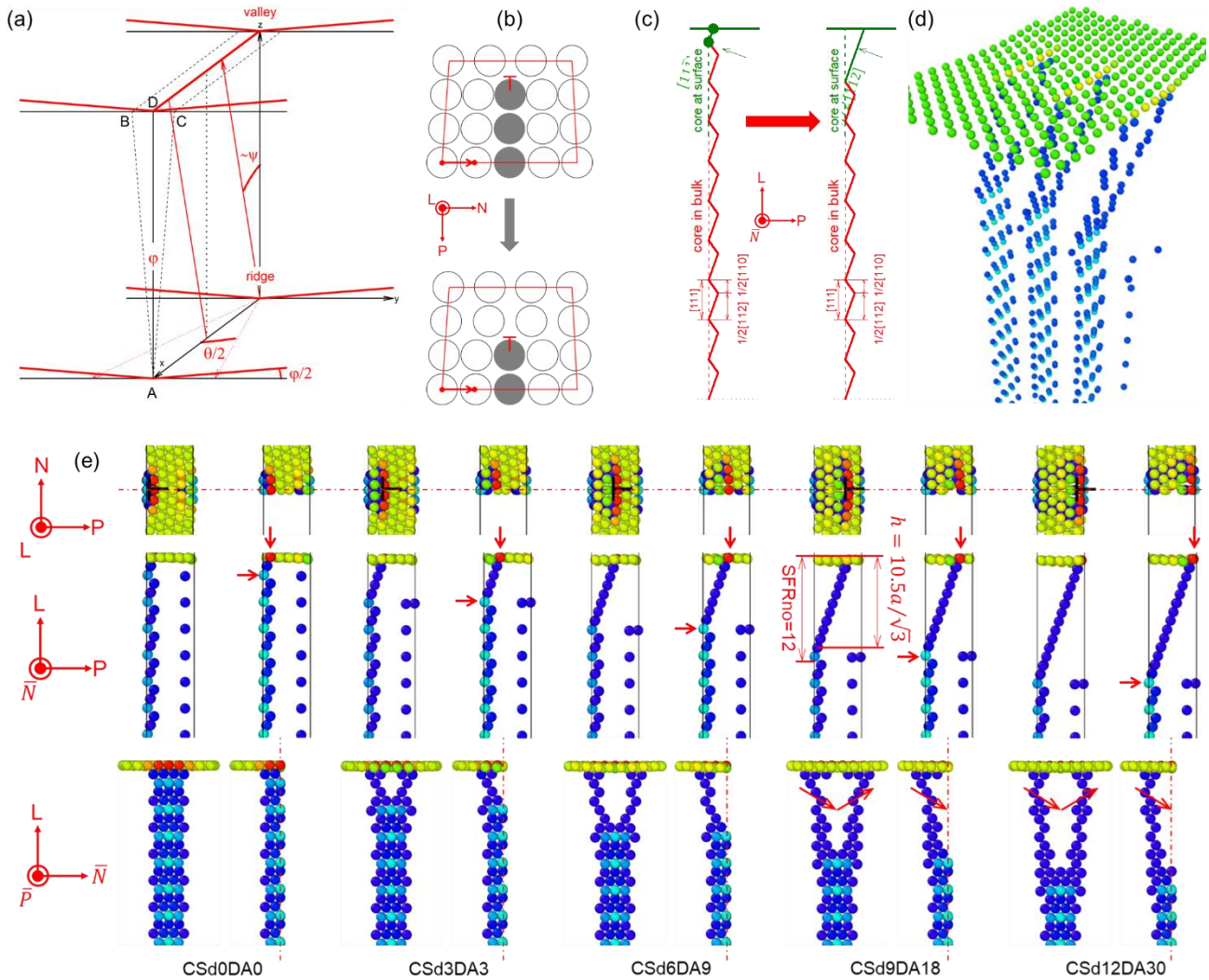
4. Conclusion

In conclusion, by extending the core-shift method to the metastable eGB structures, we found the stable eGB structures from all possible metastable structures at various core-shift depths. We further identified the zipped Y-shaped notch as the stable eGB structure. Through machine learning methods and test on additional GBs, we verified the universality of the above conclusions. We also revealed that the delocalization of the stress concentration singularity promotes the transformation of the eGB structure from the zipped V-shaped notch to the zipped Y-shaped notch. Moreover, this strongly supports the presence of restructured emergent boundaries corresponding to a zipped Y-shaped notch in (111) texture films subjected to external fields. Our research helps understand the surface-assisted GB phase transformation, stress localization and failure in thin films. It also helps analyze kinetic processes, such as dislocation climb and GB diffusion, and related local stress relaxation. Finally, it demonstrates via calculations and visualization for the widespread metastability of emergent boundaries in thin films and stimulates the strategies for related material engineering [24, 27, 28, 72-77].

Acknowledgements

X.Z. and Y.F. acknowledge the funding support from National Natural Science Foundation of China (Grant No. 52573361). X.Z. are grateful to Jian Han from City University of Hong Kong and Jinbo Yang from Zhejiang University for helpful discussion. J.J.B and I. D. acknowledge the support from Science Foundation Ireland (Grants No. 12/RC/2278_2).

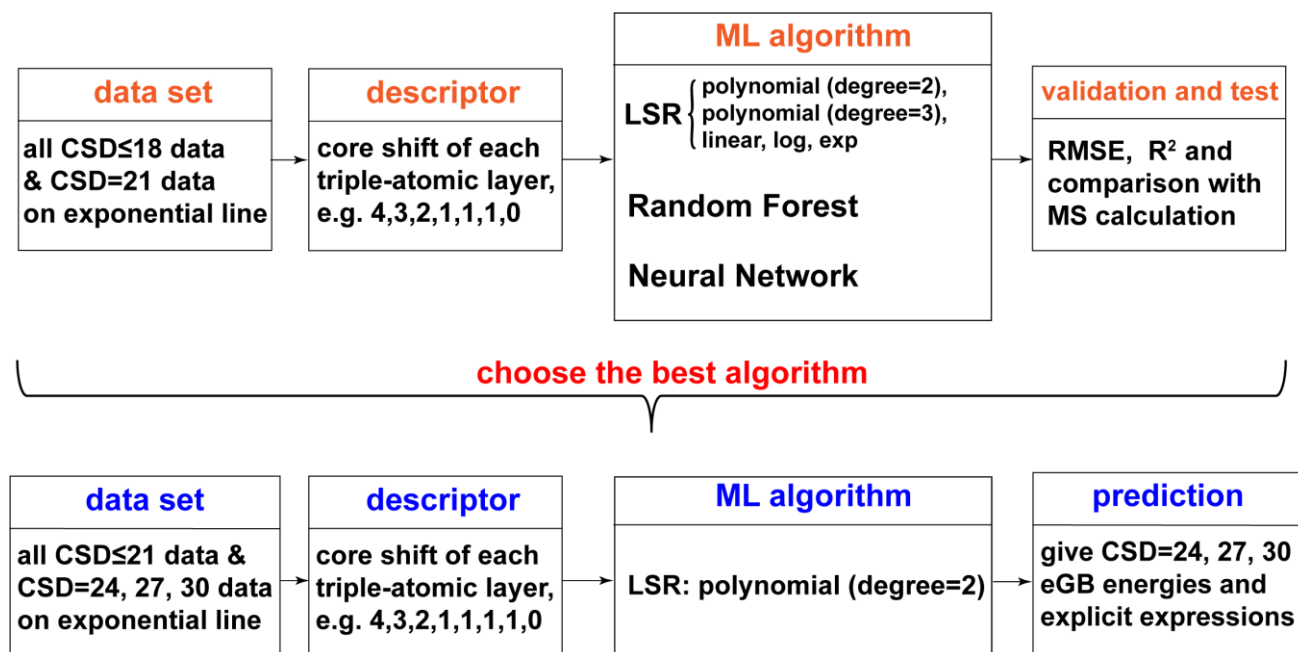
Figure 1 core-shift method to build emergent GBs



(a) out-of-plane rotation along the x axis of a bicrystal with $[111]$ axis and misorientation angle θ , and consequent core shift from $[111]$ toward $[112]$ and even further in the $(\bar{1}\bar{1}0)$ plane. (b) atomically the core-shift in a plane perpendicular to the dislocation sense vector corresponds to removing or adding one atom. L goes along tilt axis $[111]$. P is the period vector. N is the boundary normal. (c) deleting two atoms in the left image shifts the boundary core to the configuration shown in the right image. (d) perspective view of core-shifted GB with core-shift depth (CSd) 9 atom layer deep and 18 deleted atoms (DA) in total, corresponding to CSd9DA18. (e) core-shifted GB $[111]$ 13.17° step by step to build $[112]$ core shifted emergent GBs from CSd0DA0 to CSd12DA30. The top, middle and bottom panels are projected along the rotation axis L, the boundary normal N and the period vector P, respective. The cross-section is also shown after each three-view visualization. The atoms between

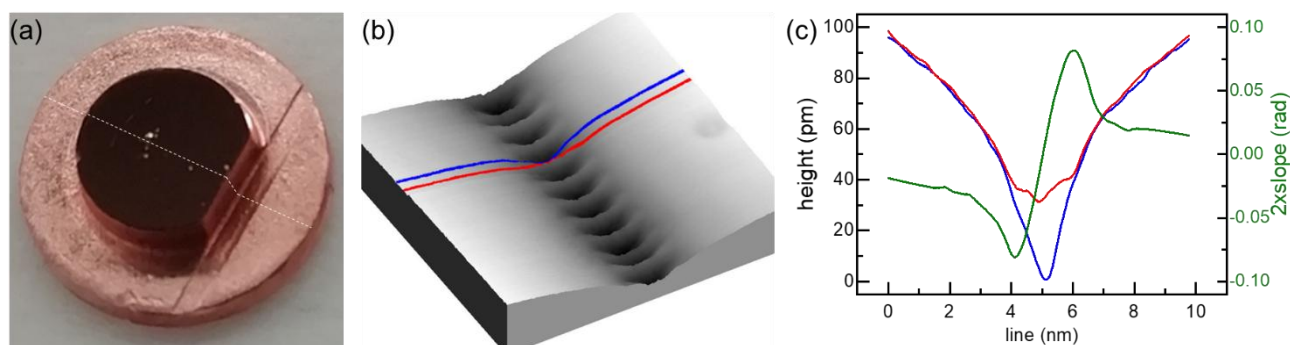
two red arrows were deleted for the atomic coordinate relaxation and then the relaxation of simulation cell sizes. The atoms are selected out with the cohesive energy higher than -3.466eV , in contrast to the cohesive energy in bulk $\sim -3.54\text{eV}$, and hence only the defective atoms were shown.

Figure 2 machine learning method



The method can be divided into two main steps. The first step includes data collection, feature selection, test of different algorithm, machine learning training and evaluation. The second one is to make prediction with the developed machine learning model.

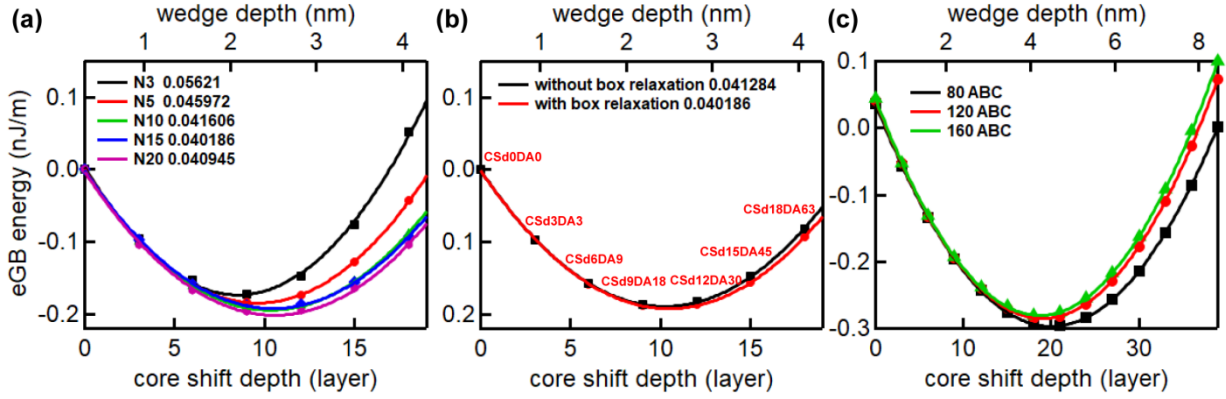
Figure 3 grain boundary structures at nanoscale



(a) macroscopic bicrystal of GB [111] 13.17° with diameter 8 mm and thickness 2mm. The intersection between the grain boundary and the surface is shown schematically as a white line. (b) Perspective view of the surface across the grain boundary at nanometer scale. The imaging condition

of scanning tunneling microscope is $I_t = 20 \text{ pA}$ and $U = -0.01 \text{ V}$. (c) topographic profile of two lines in (b) and two times of the local slope of the blue line.

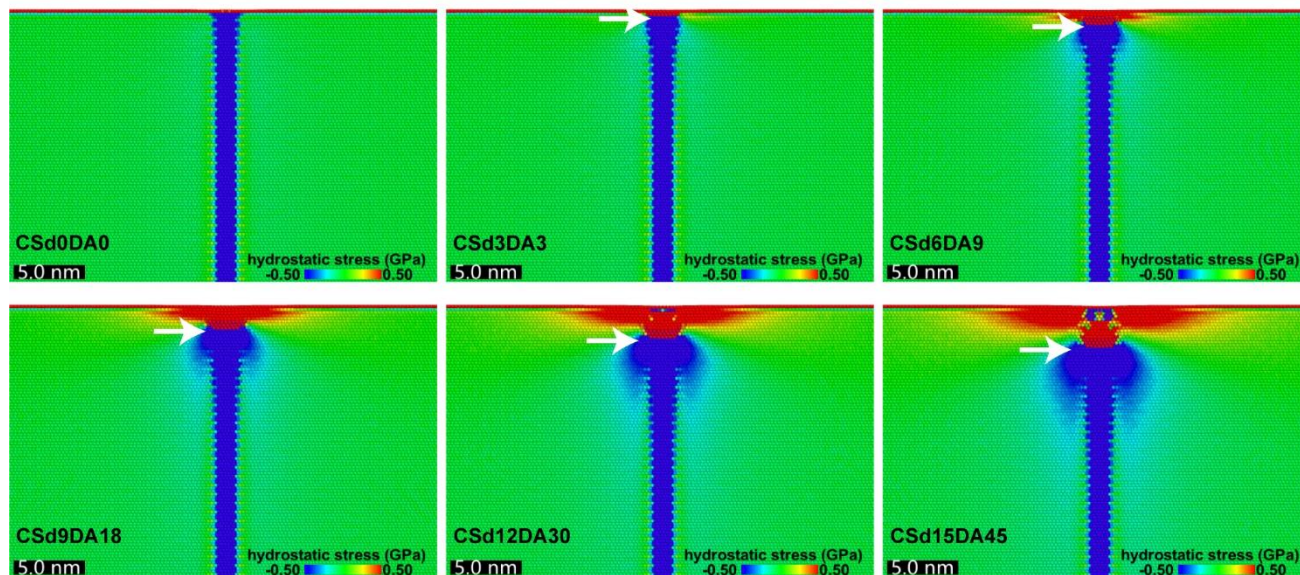
Figure 4 effect of the simulation supercell size and its relaxation on eGB energy



(a) the eGB energy for GB [111] 13.17° as a function of core-shift depth CSd and the corresponding wedge depth, $h = (CSd + 1.5) \cdot a/\sqrt{3}$ (see the upper horizontal axis) for different simulation cell size along the boundary normal with the relaxation of the simulation cell length along the boundary normal. (b) the dependence of the eGB energy for GB [111] 13.17° on the core-shift depth CSd and its corresponding wedge depth $h = (CSd + 1.5) \cdot a/\sqrt{3}$ (see the upper horizontal axis) with and without the relaxation along the boundary normal direction. (c) the dependence of the eGB energy for

GB [111] 9.43° on the wedge depth for three different film thickness, 80 ABC stacking unit, 120 ABC stacking unit and 160 ABC stacking unit.

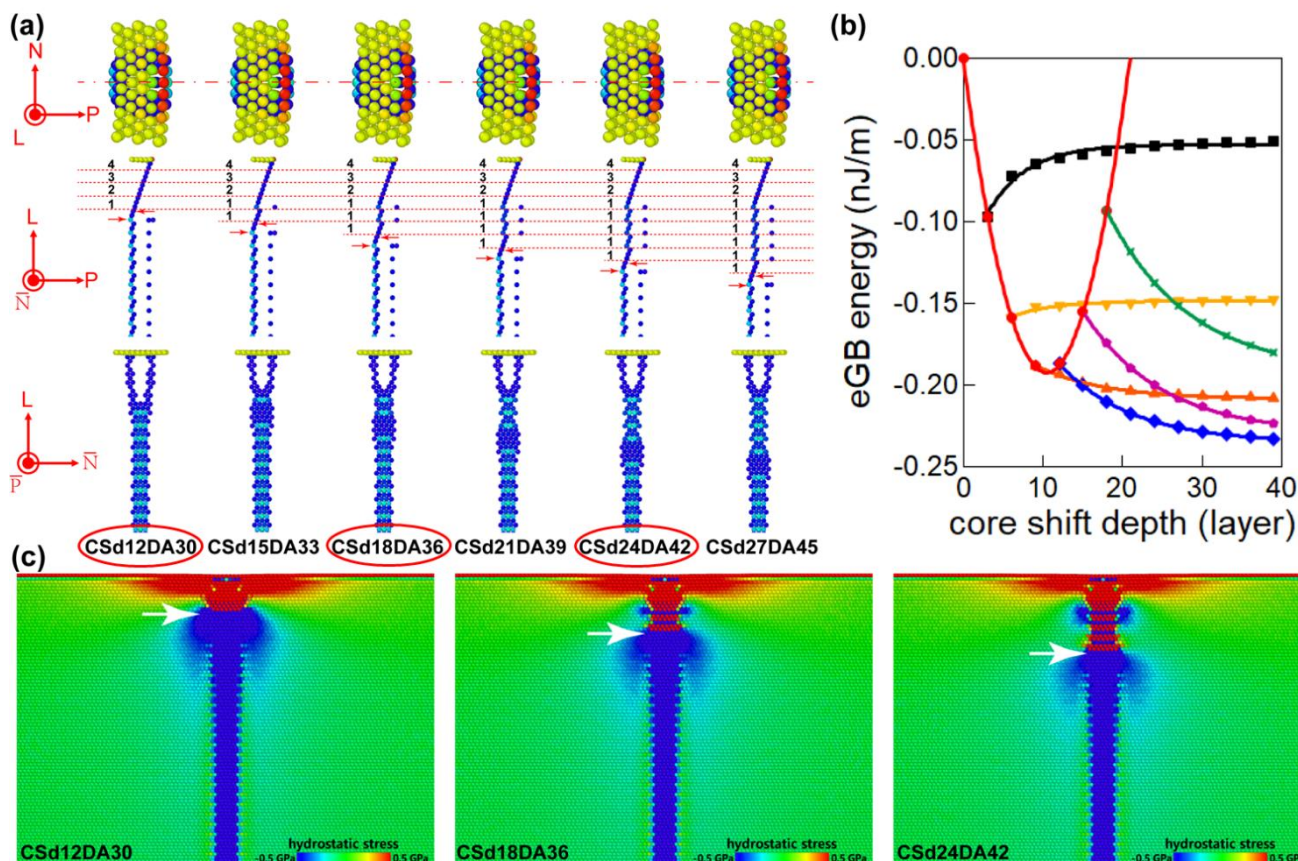
Figure 5 virial stress distribution of the core-shifted GB



The atomic stress is calculated for the core-shifted GBs with the boundary core at the free surface along [112] direction and that deep in the bulk along [111] direction. The core-shift depth means the

number of layers where atoms were deleted and the boundary cores were shifted toward [112]. (update the notation)

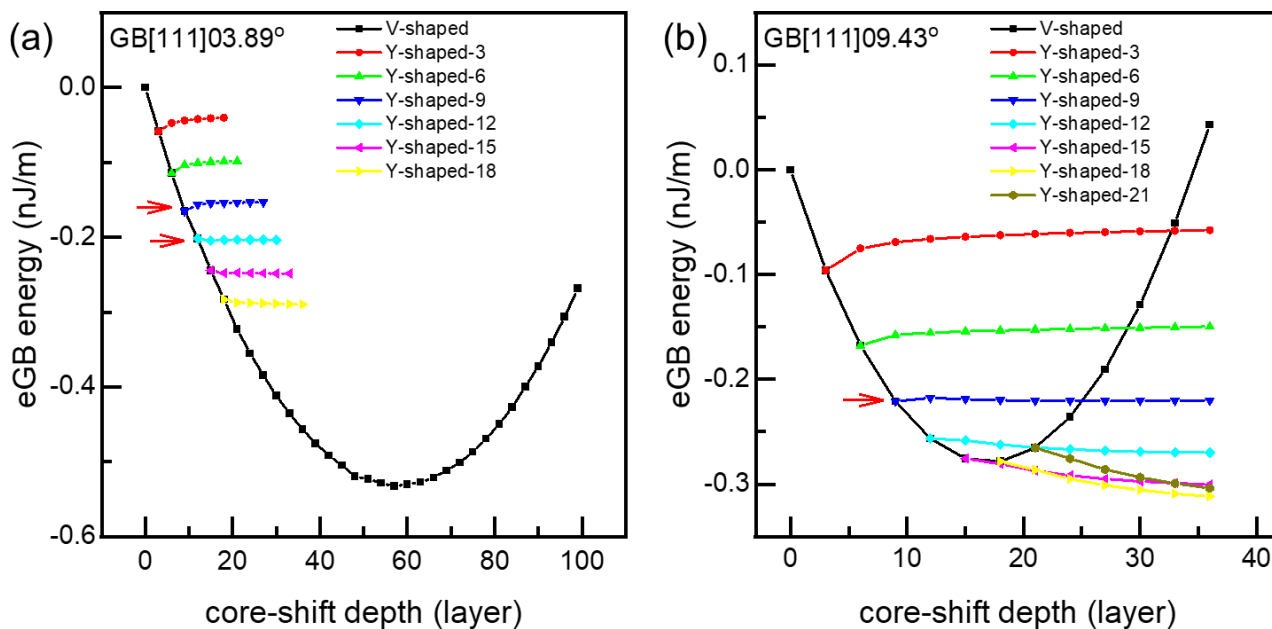
Figure 6 build structures to delocalize the stress and CSd dependent eGB energy



(a) the wedge tip blunting process with the core-shift method starting from CSd12DA30. The top, middle and the bottom panels are viewed along rotation axis, boundary normal, and period vector direction, respectively. The dot line in the middle panel lies just below the top 12 atomic layers. The rest eGB structures were obtained by core-shift further step by step through deleting the 3 atoms between two red arrows each time. Atoms are selected out by the cohesive energy greater than -3.47eV and hence only defect atoms are shown. The eGB energy for this list of structure was shown as the blue line in (b). The energy variation for other wedge tip blunting process beginning with corresponding [112] core-shifted eGBs, such as those shown in Fig. 1a, was also plotted out in (b). The energy for the [112] core-shifted eGBs were also drawn out as the red line. (c) the calculated

atomic hydrostatic stress for three eGB structures, CSd12DA30, CSd18DA36, and CSd24DA42, which were shown in (a).

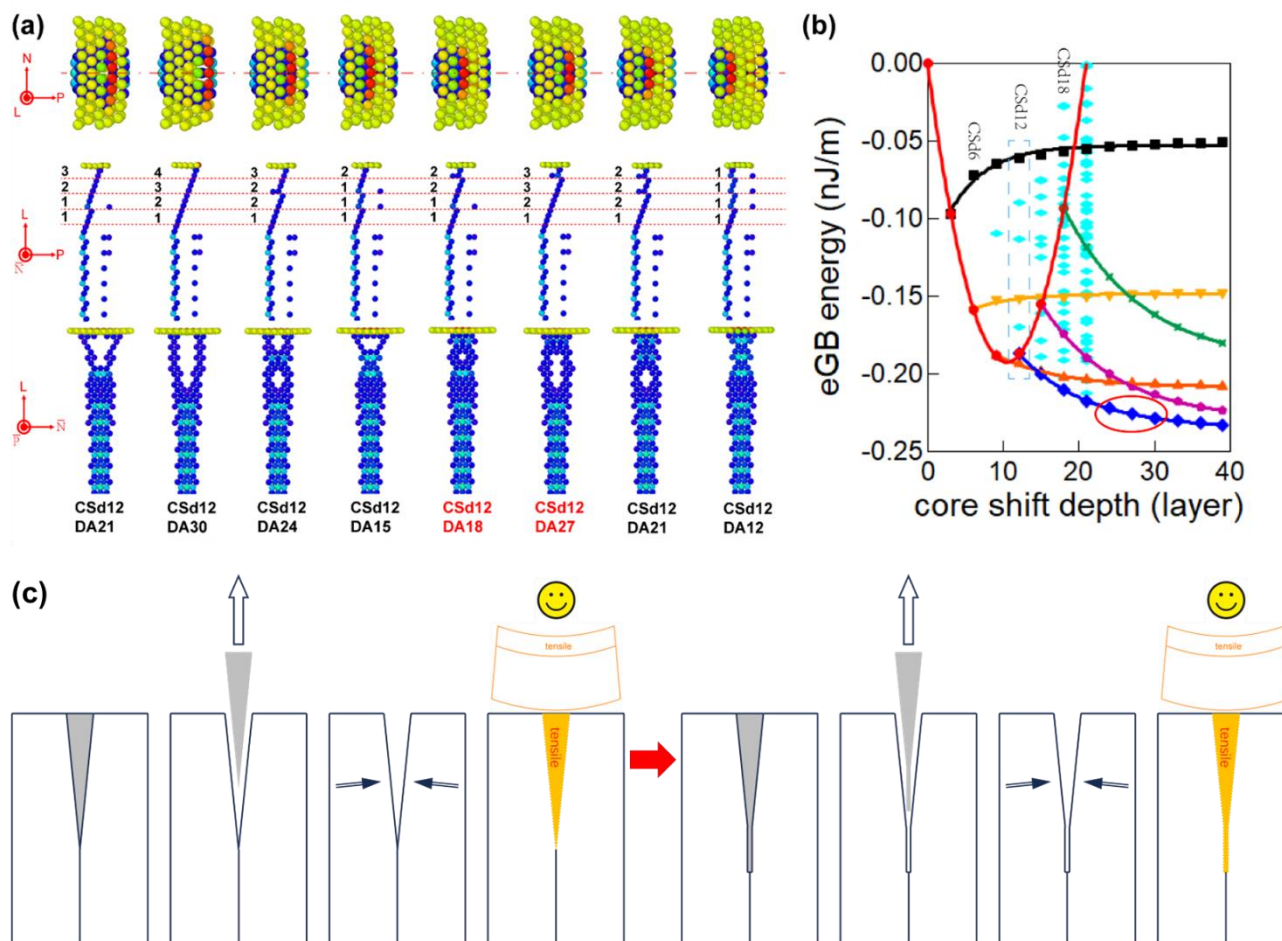
Figure 7 surface effect and crack-like singular stress concentration



A plot of the eGB energy over core-shift depth. The points on the parabolic curve corresponds to [112] core shift grain boundaries. All other curves are fitted to the exponential formula. Each point on the exponential lines apart from the intersection points with the parabolic curve corresponds to one zipped

Y-shaped notch, built from the same zipped chevron V-shaped notch through blunting the wedge tip as shown in Fig. 6a.

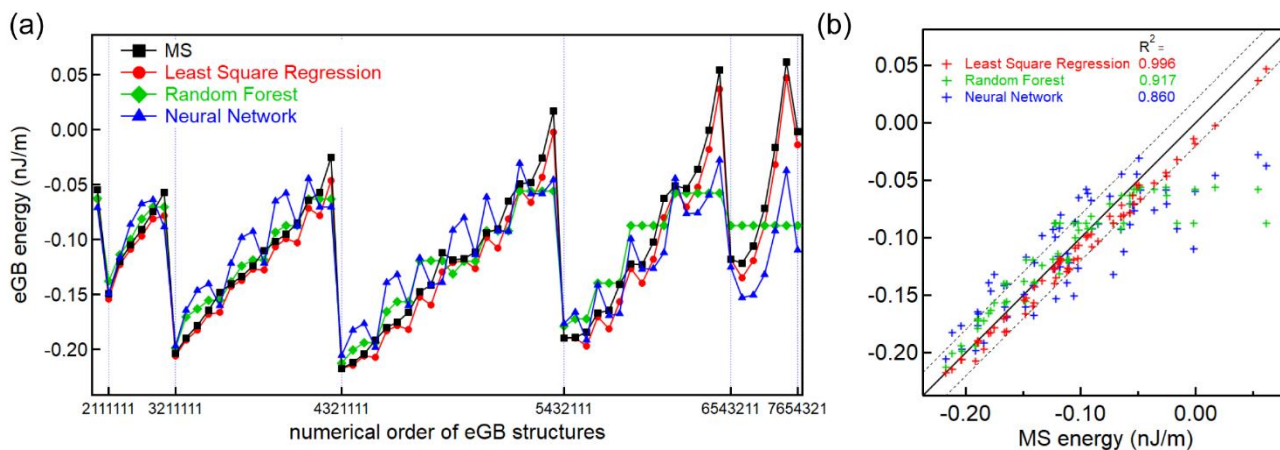
Figure 8 balance of the boundary energy and the elastic energy at a certain CSd



(a) a list of all the possible low energy eGB structures from the low energy to the high energy with the core-shift method at the fixed core shift depth. Note that there are two structures, CSd12DA18 and CSd12DA27, sharing almost the same eGB energy. The number of atoms deleted in each layer in different ABC stacking units were also labelled. Different ABC stacking units were separated with red dot lines. Atoms were selected out by the cohesive energy great than -3.469eV . (b) a plot of the eGB energy over core-shift depth. The $[11\bar{2}]$ core-shift eGBs follow a parabolic curve in red. The energy values for 8 eGB structures with core-shift depth 12 shown in (a) are highlighted in the rectangle in (b). (c) the continuum model for the transition of the stable eGB structure from the zipped V-shaped notch to zipped Y-shaped notch. For both the zipped V-shaped notch and the zipped Y-shaped notch,

the model includes four steps, these are initial structure, cut-out, zipping and final structure with local tensile stress. The substrate with films under tensile (compressive) stress tend to bend up (down).

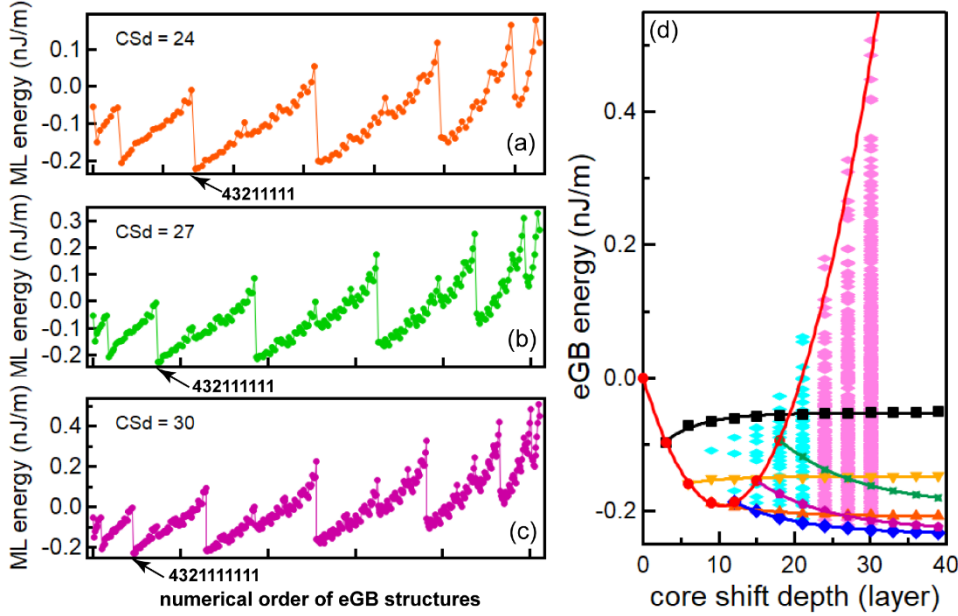
Figure 9 machine learning training and model



(a) Comparison of the eGB energy from machine learning with three different algorithms, that are neural network, random forest and least square regression (degree=2), with the calculated eGB energy with MS for CSD=21. The machine learning model is obtained from the training. The training dataset includes all the data with CSD less than 21 and the additional 6 data points on the exponential lines with CSD=21. (b) eGB results predicted from ML model as a function of the results obtained from MS.

The determination coefficient, R2 values, is for the testing data only. The solid line is the perfect fitting and dashed lines show $\pm 0.02 \text{ nJ/m}$ away from the perfect fitting.

Figure 10 machine learning model and prediction



Prediction results with least square regression (degree=2) algorithm for three different core shift depth (a) CSd=24, (b) CSd=27 and (c) CSd=30. The global minimum energies are indicated by arrows. The training dataset, from which the model is obtained, includes all the data with CSd less than 21 and the additional 6 data points on the exponential lines with CSd=24 for (a). Another 6 data points on the exponential lines with CSd=27 are added to the previous training dataset for (b). Another 12 data points on the exponential lines with CSd=27 and CSd=30 are added to the previous training dataset for (c). (d) eGB energy as a function of the core shift depth, with the predicted data included.

Table 1 analysis of the CSd dependent eGB energy

line start from \ parameters	ϵ_{ex} (nJ/m)	ξ (layer)	A (nJ/m)
CSd3DA3	-0.056412	3.62188	-0.091389
CSd6DA9	-0.15042	2.22663	-0.12605
CSd9DA18	-0.20917	8.83236	0.058499
CSd12DA30	-0.23528	9.08843	0.18116
CSd15DA45	-0.22989	9.78282	0.34613
CSd18DA63	-0.19521	10.7692	0.53898

The curve starting from different [112] core shift eGBs are fitted with an exponential formula $\epsilon = \epsilon_{ex} + A \cdot \exp(-csd/\xi)$, where ϵ_{ex} is the extrapolated value, A is the amplitude and d is the decay

length in atomic layer unit. The fitted parameters for different curves in Fig. 6b and Fig. 8b are shown below.

References

- [1] A.P. Sutton, R.W. Balluffi, *Interfaces in Crystalline Materials*, OUP Oxford 2006.
- [2] M.A. Meyers, K.K. Chawla, *Mechanical behavior of materials*, Cambridge University Press Cambridge 2009.
- [3] J.-S. Kim, J. Kim, D.-J. Yang, J. Shim, L. Hu, C.S. Lee, J. Kim, S.W. Kim, Addressing interconnect challenges for enhanced computing performance, *Science* 386(6727) (2024) eadk6189.
- [4] A.S. Saleh, K. Croes, H. Ceric, I. De Wolf, H. Zahedmanesh, A Comprehensive Microstructure-Aware Electromigration Modeling Framework; Investigation of the Impact of Trench Dimensions in Damascene Copper Interconnects, *Nanomaterials-Basel* 14(22) (2024) 1834.
- [5] M. Cesar, D.P. Liu, D. Gall, H. Guo, Calculated Resistances of Single Grain Boundaries in Copper, *Phys Rev Appl* 2(4) (2014) 044007
- [6] G.D.R. Hall, D.D.J. Allman, An evaluation of accelerated failure time models of stress-migration and stress-induced voiding failures under vias, 2015 IEEE International Reliability Physics Symposium, 2015, pp. 2D.3.1-2D.3.6.
- [7] G.D.R. Hall, D.D.J. Allman, M. Eda, T.F. Long, Engineering the failure-free lifetime for Cu vias, 2016 IEEE International Reliability Physics Symposium (IRPS), 2016, pp. 5B-4-1-5B-4-8.
- [8] N. Tuchinda, C.A. Schuh, Triple junction excess energy in polycrystalline metals, *Acta Mater* 279 (2024) 120274.
- [9] Y.-Y. Zhang, H. Xie, L.-Z. Liu, H.-J. Jin, Surface Triple Junctions Govern the Strength of a Nanoscale Solid, *Phys Rev Lett* 126(23) (2021) 235501.
- [10] R.G. Mariano, K. McKelvey, H.S. White, M.W. Kanan, Selective increase in CO₂ electroreduction activity at grain-boundary surface terminations, *Science* 358(6367) (2017) 1187-1192.
- [11] A.P. Sutton, *Concepts of Materials Science*, Oxford University Press 2021.
- [12] X. Zhang, J. Han, J.J. Plombon, A.P. Sutton, D.J. Srolovitz, J.J. Boland, Nanocrystalline copper films are never flat, *Science* 357(6349) (2017) 397-400.
- [13] J. Schiotz, K.W. Jacobsen, Nanocrystalline metals: Roughness in flatland, *Nat Mater* 16(11) (2017) 1059-1060.
- [14] X. Zhang, M. Wang, H. Wang, M. Upmanyu, J.J. Boland, Restructuring of emergent grain boundaries at free surfaces – An interplay between core stabilization and elastic stress generation, *Acta Mater* 242 (2023) 118432.
- [15] J. Han, V. Vitek, D.J. Srolovitz, Grain-boundary metastability and its statistical properties, *Acta Mater* 104 (2016) 259-273.
- [16] P.R. Cantwell, T. Frolov, T.J. Rupert, A.R. Krause, C.J. Marvel, G.S. Rohrer, J.M. Rickman, M.P. Harmer, Grain Boundary Complexion Transitions, *Annu Rev Mater Res* 50(1) (2020) 465-492.
- [17] Y. Wang, Z. Xu, V. Muralikrishnan, J.B. Harley, M.R. Tonks, G.S. Rohrer, A.R. Krause, 4D Observations of the initiation of abnormal grain growth in commercially pure Ni, *Scripta Mater* 264 (2025) 116715.
- [18] M.P. Harmer, G.S. Rohrer, Grain boundary complexions - current status and future directions, *Curr Opin Solid St M* 20(5) (2016) Iv-V.
- [19] G.S. Rohrer, The role of grain boundary energy in grain boundary complexion transitions, *Curr Opin Solid St M* 20(5) (2016) 231-239.
- [20] P.R. Cantwell, M. Tang, S.J. Dillon, J. Luo, G.S. Rohrer, M.P. Harmer, Grain boundary complexions, *Acta Mater* 62 (2014) 1-48.
- [21] T. Meiners, T. Frolov, R.E. Rudd, G. Dehm, C.H. Liebscher, Observations of grain-boundary phase transformations in an elemental metal, *Nature* 579(7799) (2020) 375-378.

- [22] L. Frommeyer, T. Brink, R. Freitas, T. Frolov, G. Dehm, C.H. Liebscher, Dual phase patterning during a congruent grain boundary phase transition in elemental copper, *Nat Commun* 13(1) (2022) 3331.
- [23] T. Frolov, D.L. Olmsted, M. Asta, Y. Mishin, Structural phase transformations in metallic grain boundaries, *Nat Commun* 4 (2013) 1899.
- [24] R. Schweinfest, A.T. Paxton, M.W. Finnis, Bismuth embrittlement of copper is an atomic size effect, *Nature* 432(7020) (2004) 1008-11.
- [25] G. Duscher, M.F. Chisholm, U. Alber, M. Ruhle, Bismuth-induced embrittlement of copper grain boundaries, *Nat Mater* 3(9) (2004) 621-6.
- [26] X. Chen, W. Goncalves, Y. Hu, Y. Gao, P. Harrison, G. Dehm, B. Gault, W. Ludwig, E. Rauch, X. Zhou, D. Raabe, Secondary grain boundary dislocations alter segregation energy spectra, *Nat Commun* 16(1) (2025) 8422.
- [27] X. Zhou, S. Kumar, S. Zhang, X. Chen, B. Gault, G. Dehm, T. Hickel, D. Raabe, Boron triggers grain boundary structural transformation in steel, *Nat Commun* 16(1) (2025) 6927.
- [28] X. Zhou, A. Ahmadian, B. Gault, C. Ophus, C.H. Liebscher, G. Dehm, D. Raabe, Atomic motifs govern the decoration of grain boundaries by interstitial solutes, *Nat Commun* 14(1) (2023) 3535.
- [29] S. Pemma, R. Janisch, G. Dehm, T. Brink, Effect of the atomic structure of complexions on the active disconnection mode during shear-coupled grain boundary motion, *Physical Review Materials* 8(6) (2024) 063602.
- [30] T. Frolov, S.V. Divinski, M. Asta, Y. Mishin, Effect of interface phase transformations on diffusion and segregation in high-angle grain boundaries, *Phys Rev Lett* 110(25) (2013) 255502.
- [31] X.P. Zhang, I. Demirel, J.J. Boland, Wedge disclination description of emergent core-shifted grain boundaries at free surfaces, *Scripta Mater* 234 (2023) 115562.
- [32] L.B. Freund, S. Suresh, *Thin Film Materials: Stress, Defect Formation and Surface Evolution*, Cambridge University Press 2004.
- [33] X. Zhang, J.J. Boland, Universal preference for low-energy core-shifted grain boundaries at the surfaces of fcc metals, *Physical Review Research* 5(1) (2023) 013223.
- [34] H. Gao, L. Zhang, W.D. Nix, C.V. Thompson, E. Arzt, Crack-like grain-boundary diffusion wedges in thin metal films, *Acta Mater* 47(10) (1999) 2865-2878.
- [35] L. Zhang, H. Gao, Coupled grain boundary and surface diffusion in a polycrystalline thin film constrained by substrate, *Int J Mater Res* 93(5) (2002) 417-427.
- [36] M.J. Buehler, A. Hartmaier, H. Gao, Constrained Grain Boundary Diffusion in Thin Copper Films, *MRS Online Proceedings Library* 821(1) (2004) 36-47.
- [37] L. Wang, J. Teng, P. Liu, A. Hirata, E. Ma, Z. Zhang, M. Chen, X. Han, Grain rotation mediated by grain boundary dislocations in nanocrystalline platinum, *Nat Commun* 5 (2014) 4402.
- [38] M. Wang, R. Yan, X. Han, H. Wang, M. Upmanyu, Emergent grain boundary phases in stressed polycrystalline thin films, *Physical Review Materials* 7(8) (2023) 083602.
- [39] M.J. Buehler, H. Yao, H. Gao, B. Ji, Cracking and adhesion at small scales: atomistic and continuum studies of flaw tolerant nanostructures, *Model Simul Mater Sc* 14(5) (2006) 799.
- [40] C. Wang, K. Du, K. Song, X. Ye, L. Qi, S. He, D. Tang, N. Lu, H. Jin, F. Li, H. Ye, Size-Dependent Grain-Boundary Structure with Improved Conductive and Mechanical Stabilities in Sub-10-nm Gold Crystals, *Phys Rev Lett* 120(18) (2018) 186102.
- [41] P. Liu, S.C. Mao, L.H. Wang, X.D. Han, Z. Zhang, Direct dynamic atomic mechanisms of strain-induced grain rotation in nanocrystalline, textured, columnar-structured thin gold films, *Scripta Mater* 64(4) (2011) 343-346.
- [42] S.F. Chu, P. Liu, Y. Zhang, X.D. Wang, S.X. Song, T. Zhu, Z. Zhang, X.D. Han, B.D. Sun, M.W. Chen, In situ atomic-scale observation of dislocation climb and grain boundary evolution in nanostructured metal, *Nat Commun* 13(1) (2022).
- [43] T.J. Balk, G. Dehm, E. Arzt, Parallel glide: unexpected dislocation motion parallel to the substrate in ultrathin copper films, *Acta Mater* 51(15) (2003) 4471-4485.
- [44] S. Plimpton, Fast Parallel Algorithms for Short-Range Molecular-Dynamics, *J Comput Phys* 117(1) (1995) 1-19.

- [45] Y. Mishin, M.J. Mehl, D.A. Papaconstantopoulos, A.F. Voter, J.D. Kress, Structural stability and lattice defects in copper: Ab initio, tight-binding, and embedded-atom calculations, *Phys Rev B* 63(22) (2001) 224106.
- [46] A.P. Thompson, S.J. Plimpton, W. Mattson, General formulation of pressure and stress tensor for arbitrary many-body interaction potentials under periodic boundary conditions, *J Chem Phys* 131(15) (2009).
- [47] A. Stukowski, Visualization and analysis of atomistic simulation data with OVITO-the Open Visualization Tool, *Model Simul Mater Sc* 18(1) (2010) 015012.
- [48] M.A. Tschopp, D.L. McDowell, Asymmetric tilt grain boundary structure and energy in copper and aluminium, *Philos Mag* 87(25) (2007) 3871-3892.
- [49] K.N. Sasidhar, N.H. Siboni, J.R. Mianroodi, M. Rohwerder, J. Neugebauer, D. Raabe, Enhancing corrosion-resistant alloy design through natural language processing and deep learning, *Science Advances* 9(32) (2023) eadg7992.
- [50] J. Xiong, S.-Q. Shi, T.-Y. Zhang, Machine learning of phases and mechanical properties in complex concentrated alloys, *J Mater Sci Technol* 87 (2021) 133-142.
- [51] N. Ran, B. Sun, W. Qiu, E. Song, T. Chen, J. Liu, Identifying Metallic Transition-Metal Dichalcogenides for Hydrogen Evolution through Multilevel High-Throughput Calculations and Machine Learning, *The Journal of Physical Chemistry Letters* 12(8) (2021) 2102-2111.
- [52] Y. Cui, H.B. Chew, Machine-Learning Prediction of Atomistic Stress along Grain Boundaries, *Acta Mater* 222 (2022) 117387.
- [53] C.W. Rosenbrock, E.R. Homer, G. Csanyi, G.L.W. Hart, Discovering the building blocks of atomic systems using machine learning: application to grain boundaries, *npj Computational Materials* 3 (2017) 1.
- [54] C.B. Owens, N. Mathew, T.W. Olaveson, J.P. Tavenner, E.M. Kober, G.J. Tucker, G.L.W. Hart, E.R. Homer, Feature engineering descriptors, transforms, and machine learning for grain boundaries and variable-sized atom clusters, *npj Computational Materials* 11(1) (2025) 21.
- [55] W. Ye, H. Zheng, C. Chen, S.P. Ong, A Universal Machine Learning Model for Elemental Grain Boundary Energies, *Scripta Mater* 218 (2022) 114803.
- [56] X. Zhou, Y. Wei, M. Kühbach, H. Zhao, F. Vogel, R. Darvishi Kamachali, G.B. Thompson, D. Raabe, B. Gault, Revealing in-plane grain boundary composition features through machine learning from atom probe tomography data, *Acta Mater* 226 (2022) 117633.
- [57] F. Pedregosa, G. Varoquaux, A. Gramfort, V. Michel, B. Thirion, O. Grisel, M. Blondel, P. Prettenhofer, R. Weiss, V. Dubourg, Scikit-learn: Machine Learning in Python, *Journal of Machine Learning Research* (2011).
- [58] J.S. Tello, A.F. Bower, E. Chason, B.W. Sheldon, Kinetic model of stress evolution during coalescence and growth of polycrystalline thin films, *Phys Rev Lett* 98(21) (2007) 216104.
- [59] E. Vasco, M.J. Ramírez-Peral, A. Jacas-Rodríguez, C. Polop, Kinetics of intrinsic stress in nanocrystalline films, *Scripta Mater* 202 (2021) 114015.
- [60] M.J. Buehler, H. Gao, Dynamical fracture instabilities due to local hyperelasticity at crack tips, *Nature* 439(7074) (2006) 307-310.
- [61] M.J. Buehler, F.F. Abraham, H. Gao, Hyperelasticity governs dynamic fracture at a critical length scale, *Nature* 426(6963) (2003) 141-146.
- [62] J.P. Hirth, J. Lothe, *Theory of Dislocations*, McGraw-Hill 1982.
- [63] D. Hull, D.J. Bacon, *Introduction to dislocations*, Elsevier 2011.
- [64] W.D. Nix, B.M. Clemens, Crystallite coalescence: A mechanism for intrinsic tensile stresses in thin films, *J Mater Res* 14(8) (1999) 3467-3473.
- [65] E. Chason, B.W. Sheldon, L.B. Freund, J.A. Floro, S.J. Hearne, Origin of compressive residual stress in polycrystalline thin films, *Phys Rev Lett* 88(15) (2002) 156103.
- [66] J.A. Floro, E. Chason, R.C. Cammarata, D.J. Srolovitz, Physical origins of intrinsic stresses in Volmer-Weber thin films, *Mrs Bull* 27(1) (2002) 19-25.
- [67] Q. Zhu, A. Samanta, B. Li, R.E. Rudd, T. Frolov, Predicting phase behavior of grain boundaries with evolutionary search and machine learning, *Nat Commun* 9(1) (2018) 467.

- [68] T. Frolov, M. Asta, Y. Mishin, Phase transformations at interfaces: Observations from atomistic modeling, *Curr Opin Solid St M* 20(5) (2016) 308-315.
- [69] R.W. Hoffman, Stresses in Thin-Films - Relevance of Grain-Boundaries and Impurities, *Thin Solid Films* 34(2) (1976) 185-190.
- [70] L.B. Freund, E. Chason, Model for stress generated upon contact of neighboring islands on the surface of a substrate, *J Appl Phys* 89(9) (2001) 4866-4873.
- [71] A.A. Griffith, The phenomena of rupture and flow in solids, *Philosophical transactions of the royal society of london. Series A, containing papers of a mathematical or physical character* (1921) 163-198.
- [72] A. Ahmadian, D. Scheiber, X. Zhou, B. Gault, C.H. Liebscher, L. Romaner, G. Dehm, Aluminum depletion induced by co-segregation of carbon and boron in a bcc-iron grain boundary, *Nat Commun* 12(1) (2021) 6008.
- [73] N.J. Peter, T. Frolov, M.J. Duarte, R. Hadian, C. Ophus, C. Kirchlechner, C.H. Liebscher, G. Dehm, Segregation-Induced Nanofaceting Transition at an Asymmetric Tilt Grain Boundary in Copper, *Phys Rev Lett* 121(25) (2018) 255502.
- [74] Z. Yu, P.R. Cantwell, Q. Gao, D. Yin, Y. Zhang, N. Zhou, G.S. Rohrer, M. Widom, J. Luo, M.P. Harmer, Segregation-induced ordered superstructures at general grain boundaries in a nickel-bismuth alloy, *Science* 358(6359) (2017) 97-101.
- [75] K.M. Yin, A.H. King, T.E. Hsieh, F.R. Chen, J.J. Kai, L. Chang, Segregation of bismuth to triple junctions in copper, *Microsc Microanal* 3(5) (1997) 417-422.
- [76] U. Alber, H. Mullejons, M. Ruhle, Bismuth segregation at copper grain boundaries, *Acta Mater* 47(15-16) (1999) 4047-4060.
- [77] M. Kuzmina, M. Herbig, D. Ponge, S. Sandlobes, D. Raabe, Linear complexions: Confined chemical and structural states at dislocations, *Science* 349(6252) (2015) 1080-3.